Advances in Geosciences
Vol. 15: Planetary Science (2007)
Eds. Anil Bhardwaj *et al.*

THE STEREO CAMERA ON THE BEPICOLOMBO ESA/JAXA MISSION: A NOVEL APPROACH

GABRIELE CREMONESE, DANIELA FANTINEL
and ENRICO GIRO
INAF — Osservatorio Astronomico
vic. Osservatorio 5, Padova, Italy

MARIA TERESA CAPRIA
INAF — IASF, Roma, Italy

VANIA DA DEPPO and GIAMPIERO NALETTO
Dipartimento di Ingegneria dell'Informazione
Universita' di Padova, Padova, Italy
CNR/INFM/LUXOR, Padova, Italy

GIANFRANCO FORLANI
Dipartimento di Ingegneria civile
Universita' di Parma, Parma, Italy

MATTEO MASSIRONI and LORENZA GIACOMINI
Dipartimento di Geoscienze
Universita' di Padova, Padova, Italy

MARIA SGAVETTI
Dipartimento di Scienza della Terra
Universita' di Parma, Parma, Italy

EMANUELE SIMIONI, STEFANO DEBEI, CARLO BETTANINI,
MIRCO ZACCARIOTTO and PATRIZIA BORIN
CISAS, Universita' di Padova, Padova, Italy

LUCIA MARINANGELI
IRSPS, Universita' di Pescara, Pescara, Italy

LUCIANO CALAMAI
Galileo Avionica S.p.A., Campi Bisenzio, Firenze, Italy

ENRICO FLAMINI
ASI, Roma, Italy

The stereo camera (STC) is one of three channels of the spectrometer and imagers for Mercury Planet Orbiter BepiColombo Integrated Observatory SYStem (SIMBIOSYS), which will be on board the Mercury Planetary Orbiter of the ESA mission BepiColombo. SIMBIOSYS includes also an high resolution imaging channel (HRIC), providing images at spatial resolution of 5 m/pixel at the periherm, and the VIS-NIR spectrometer (VIHI) that will provide the global mapping of the Mercury's surface in the spectral range 400–2200 nm, with a spectral sampling of 6.25 nm, and the spatial resolution of 400 m/pixel at the periherm. The main scientific objective of STC is the global mapping of the entire surface of the Mercury in 3D and colors with a scale factor of 50 m/pixel at the periherm. It will allow to generate the digital terrain model (DTM) of the entire surface improving the interpretation of morphological features at different scales and topographic relationships.

The harsh environment of the Mercury will strongly affect the functionalities and performance of the instruments reducing the resources allocated to the payload. Even for the stereo camera, as for most of the instrument on board BepiColombo, a novel design had to be considered.

We have implemented an original optical design, modifying a classical configurations, and a new technique of acquiring the stereo pairs for generating the DTM of the surface. The new technique will have an impact on the software chain generating the DTM and on the observation strategy.

The stereo camera consists of two channels, looking at the surface at $\pm 20^\circ$ from the nadir direction, converging on the same bidimensional focal plane assembly, with no mechanical movable parts. The configuration of the focal plane assembly allows to apply the push-frame technique to acquire the stereo images.

1. Introduction

BepiColombo is the fifth cornerstone mission of the European Space Agency (ESA) and it has the aim of studying in great detail the innermost of the Solar System planets: Mercury.

Mercury is very important from the point of view of testing and constraining the dynamical and compositional theories of planetary system formation.

In fact, being in close proximity to the Sun, it has been affected by a rather peculiar environment, such as the high temperature and the large diurnal variation, the rotational state changes due to the tidal deformation induced by the Sun, the surface alteration during the cooling phase, and the chemical surface composition modified by the bombardment.

Mercury was closely observed only by the Mariner 10 spacecraft in 1974–1975 and about 45% of Mercury's surface was acquired with a spatial resolution between 1 km and 1.5 km, whereby <1% was covered at a resolution between 100 m and 500 m[1–3] and some measurements of the planet magnetic field were done.

The BepiColombo mission, especially designed to fully characterize the planet, will consists of two modules: a Mercury Planet Orbiter (MPO) carrying the remote sensing and the radio science experiments, and a Mercury Magnetospheric Orbiter (MMO), carrying the field and particle science instrumentation. The two complementary packages will allow to map the entire surface of the planet and to study the magnetosphere and its relation with the surface, the exosphere, and the interplanetary medium.

To achieve the mission objectives, the orbits of the two modules are rather different: MMO will be put in a highly elliptical polar orbit with the periherm and the apoherm altitudes of 400 and 12,000 km, respectively; the MPO will be in a slightly elliptical polar orbit with the periherm and the apoherm altitudes of 400 km and 1,500 km and with the orbital period of 2.3 h.

The MPO orbital characteristics are determined in order to image the whole surface of Mercury at medium resolution during the one year nominal mission lifetime, and because of the extremely challenging thermal constraints on the spacecraft (S/C). For a continuous observation of the planet surface during the mission, the S/C is three-axis stabilized with the Z-axis, corresponding to payload boresight direction, pointing to the nadir direction.

The launch of the mission is foreseen in August 2013, and the S/C will reach Mercury in August 2019, after one Moon, one Earth, two Venus, and two Mercury flybys.

2. Scientific Objectives

Mercury is the most enigmatic planet of the inner Solar System and can be defined as an end-member since, being the closest to the Sun, it can give important information on the origin and evolution of the Solar System. The lack of data about the majority of the Mercury surface leaves many open questions regarding crustal differentiation, resurfacing, volcanism, tectonics, and surface/atmosphere interaction. Some of these topics can be successfully addressed by the data that the Stereo imaging Channel (STC) on board BepiColombo will acquire.

2.1. *Mercury's surface composition*

The surface composition of a planet is the mirror of its evolution and, in particular, it reflects its crustal differentiation. In addition, for Mercury it is

also crucial to unambiguously identify the source minerals of its exosphere constituents. Unfortunately, the determination of surface composition of Mercury from ground-based observations is very difficult due to the observational constraints imposed by the small solar elongation of the planet. In addition, the Mercury surface spectrum is likely affected by space weathering greatly enhanced by the close proximity to the Sun and the high meteoroid impact velocities.[2,4–6] As a consequence, even if from the mid-90s onwards several valuable works have been published on visible, near and mid-infrared spectroscopy of the hermean surface, the mineralogical, chemical and isotopic composition of Mercury's surface is still poorly constrained.[1–3]

The comparison of the hermean spectra with the lunar highlands and with the laboratory studies of terrestrial, lunar, and meteoritic materials indicates that the Mercury surface is dominated by a low Fe-anorthosite.[7,8] Nonetheless near and mid-infrared spectroscopy has proven a wide heterogeneity of the hermean surface mineralogical composition. Actually different silica content, plagioclase phases (labradorite to bytwonite) ortho- (enstatite, hypersthene) and clino-pyroxenes (augite, diopside) have been proposed and detected in different areas of the planet.[9–13] In addition, recalibrated Mariner 10 images showed compositional and soil maturity variations consistent with the presence of basaltic volcanic flows and pyroclastic deposits.[14]

The STC filters are located in the spectral range where the electronic processes in the transition elements give the major contribution to the absorption spectra of minerals. In particular, the filter locations (420, 550, 750, and 920 nm) are in proximity of Fe^{2+} absorption bands characterizing different minerals (pyroxene, garnet, olivine, oxides, and sulfides) that can be likely present in different amount in the anorthosites, basalts, and possibly norites and gabbros at the Mercury surface.[15] The color mapping of the STC will therefore allow to discriminate among rock-forming minerals primarily on the basis of the albedo and color contrasts.

2.2. *Mercury's lithostratigraphic units*

On the basis of the Mariner images, four major lithostratigraphic units have been recognized on Mercury[16,17] smooth plains, intercrater plains, heavily cratered terrains, and hilly and lineated terrains. It is very likely that other geological units will be recognized at a global scale thanks to STC color filters and better geometric resolution. The analysis and the mapping of

the lateral and the vertical contacts among the geological units will be very important to establish the sequence of events that formed and modified the crust of Mercury. Since a geological unit, defined by remote sensing, is characterized by its morphology, texture, and spectral signature, wide areas should be covered with color filters and a resolution adequate to recognize stratigraphic relationships among units. STC will constrain the relationship between different geological units in extended regions and consequently a satisfactory knowledge of the global stratigraphy will be achieved.

2.3. *Cratering record and surface age*

The cratering record is an outstanding tool for geological dating and provides important information on the origin of impacting objects.[18]

Mercury's cratering record based on Mariner 10 data suggests that the internal activity of Mercury was more extensive early in its history than that on the Moon, but ended sooner. In particular, the youngest surfaces dated through crater population are the smooth plains of the Caloris basin that were attributed to the late heavy bombardment (3.8 Ga).[2,19–21] However, the lack of knowledge about the largest part of the planetary surface and the low Mariner 10 spatial resolution yields uncertainties in the definition of the chronostratigraphic evolution of Mercury. The STC global coverage will provide the opportunity of dating the whole hermean surface. In addition, its spatial resolution (up to 50 m/pixel) will allow identification of craters with diameter larger than about 0.2 km, providing an accurate estimate of model ages through crater counting of the different hermean terrains even for very recent units. These data will be useful for the determination of the impact flux of the inner Solar System through times.

2.4. *Impact cratering*

The illuminated surface of Mercury seen during the incoming view of Mariner 10 is dominated by craters, basins, and hilly and lineated terrains, whereas the outgoing view exhibits large basins and large tracts of relatively smooth areas. The impact crater population differs in size (100 m up to at least 1300 km) and preservation degree. The STC global coverage, resolution, and 3D rendering capabilities will provide useful information on geomorphological and geological characterization of impact craters. Indeed, the morphological characteristics of these features provide important information on maturity degree, substrate properties, resurfacing

processes, and impacting objects. In addition, the determination of erosion processes and crater removal rate are important to estimate the rate of global resurfacing, still unknown on the Mercury.

A detailed analysis using the imaging channels of STC will allow the morphometric characterization of the craters and the reconstruction of the degradation sequence and post-impact tectonic deformation. In addition, the global coverage of STC will permit considerations about latitude and/or longitude dependence of the degradation processes. Depth estimation and slope stability analysis can be performed using the digital terrain model (DTM) obtained by STC.

The recent analysis of the Moon has demonstrated that the detection, the geomorphological characterization, and the depth estimate of multi-ring basins can give important information on the rheology of the ancient lithosphere and mantle.[22] In the Mariner 10 data only two structures have been identified as a multi-ring basin: Caloris (1300 km) and Tolstoj (400 km). Only recently a new large basin named Skinakas (2000 km wide) has been possibly detected through ground-based observations of the unknown portion of Mercury surface.[23]

The Caloris basin and the hilly and lineated terrains at its antipode represent as a whole one of the most significant and equally intriguing examples of tectonic events due to exogenic process in the Solar System. The most interesting characteristics of Caloris basin are the lack of a well-developed ring outside the main crater rim (Caloris Montes) and the presence of extensional grabens superimposed on compressional ridges deforming the post-impact lava plains inside the basin. The lack of well-developed external ring can be due to a thick lithosphere (over 100 km) which prevents penetration.[24] Additional explanations include topography viscous relaxation; extensive smooth plain covers, and subsidence of lithosphere ring bounded blocks.[25]

The extensional troughs cutting convex shaped ridges inside the basin have been explained through different models. The main models are: subsidence related compression during smooth plains extrusion outside Caloris followed by isostatic uplift and pellicular extension of the not yet completely compensated basin[26,27]; nearly contemporaneous extension in basin center and compression at its margin as consequence of the stress induced by annular load of the smooth plains lava deposits outside Caloris[24]; compression related to subsidence for interior plains load, followed by outer smooth plains emplacement and consequent basin center uplift and extension as a result of the annular load.[25] Fleitout and Thomas[28]

and Thomas *et al.*[29] finally take into account the stress perturbation of Caloris basin under the general contraction of the planet due to core cooling. According to this model the lithosphere motion, toward the Caloris zero stress field area, induced compression inside the basin and its surroundings preventing ring formation and favoring concentric folding (ridges) of the hot and soft inner plains; when inner lava deposits became more rigid after cooling, the persisting compression gave rise to bukling associated with pellicular extension.

The hilly and lineated terrains consist of high blocks surrounded by rectilinear depressions probably due to focusing of impact-generated seismic waves at the Caloris basin antipode.[20,24,30]

A detailed structural analysis, aided by perspective views, high resolution and/or large area coverage also of the unknown part of Mercury surface, will bring important insights on large basins evolution, focusing of seismic waves after huge impacts, post-impact plain emplacement, and deformation style.

2.5. *Volcanism*

The presence of volcanism on Mercury is still under debate. Indeed, there are evidences for a volcanic origin of some plain units,[14,31,32] but no volcanic edifices have unambiguously identified from the Mariner 10 images. However, it should be kept in mind that the low resolution of most of the Mariner 10 data set could not have revealed volcanic edifices even on the Earth. For this reason studying the volcanism on Mercury is essential among the STC scientific objectives. To correctly address this subject three main objectives have been selected.

(a) *Identification of different lava flows and volcanic deposits with definition of their emplacement mechanisms.* Lava flows are characterized by different thickness, area extent, and emplacement processes that are related to their composition, volatile content, and effusion rates. Under favorable low illumination angles the STC will be able to distinguish different lava flows and deposits on the basis of their area extension (single self-confined flows or lava sheet), characteristic surface features (tumuli, squeeze-ups, lava channels, lava ridges and rises), and composition.

(b) *Identification of volcanic edifices, domes, and dykes.* The size of volcanoes, domes, and dykes of the terrestrial planets ranges from a few hundreds of meters to hundreds of kilometers, and thus the STC resolution will allow the identification of small volcanic features as well.[33]

(c) *Identification of possible fissured vents.* A limited number of domes and volcanic features coupled with a possible extensive presence of basalt plains points at a past fissure activity that can be identified thanks to the synthetic view and the 3D rendering of STC.

2.6. *Tectonics*

On the basis of the Mariner 10 data, five types of tectonic features have been observed:

(a) a global grid network formed during equatorial bulge relaxation of controversial origin;
(b) the lobate scarps related to core cooling and associated crustal contraction;
(c) the structures connected to Caloris basin already described in Sec. 2.4:
(d) the minor structures such as rectilinear troughs, grooves and hills, linked to local tectonic events;
(e) the linear ridges of uncertain origin.

The global grid network is composed by well-developed lineaments located mainly in the ancient cratered regions (heavily cratered terrains and intercrater plains). The models proposed to explain the formation of the grid network suggest the tidal spin down and the consequent equatorial bulge relaxation[24,27,34,35]; however, the tectonic feature patterns and the directions predicted by the proposed models do not correspond to what has been observed on Mariner 10 data.[29] This doubt is due to the very partial knowledge of the Mercury surface and the strong disturb of solar illumination on image interpretations (lineaments perpendicular to solar azimuth are heavily enhanced and the parallel ones are weakly detectable). The 3D restitution obtained by STC images should lead to a global lineament mapping only slightly affected by directional interpretation errors since the STC derived DTMs will reflect more directly the morphological pattern of the surface. Therefore, the despinning models can be better constrained and the other mechanisms that changed the planet shape during the early history of its surface may be recognized.

The main tectonic features on Mercury surface are lobate scarps consisting of 20–500 km long and few 100 m to about 3 km high escarpments. They are interpreted as the surface expression of thrusts, on the basis of their asymmetric morphology and the associated compressional

displacement inferred from some displaced craters.[26,36,37] The randomly oriented lobate scarps azimuths and the lack of coeval extensional features, that can compensate the thrust related shortening, brought to the broadly accepted interpretation that the lobate scarps are the result of lithosphere contraction due to gradual planetary cooling.[24,37] Some authors noticed a slight preferred orientation of lobate scarps radial to Caloris basin in the south polar region.[28,29] This would suggest that they have been formed by a stress perturbation due to a far-field tectonic effect of Caloris basin during the overall global contraction. This intriguing hypothesis is however weakly constrained due to the paucity of stereo imaging provided by Mariner 10. Without a stereoscopic vision only sharper and younger scarps are clearly detectable and the illumination effects heavily affect image interpretation. DTMs derived from the stereoscopic channel of SIMBIOSYS will consistently improve the calculation of crustal shortening and planet radius decreasing realized up to date.[37] In addition, DTM derived cross-sections of lobate scarps can be used as references for faulting modeling to obtain accurate estimates of the fault displacement and important insights on the thickness of the elastic lithosphere at the time of faulting.

The minor structures related to local tectonic events have been identified in Tolstoj-Zeami, Phidias, and Kalidasa-Milton areas, which are not related to global tectonic events as tidal-despinning, crustal contraction by core cooling, and Caloris basin formation.[29,38] The presence of features linked to the local tectonic events affecting more or less wide areas suggests that these phenomena could be quite common in the Mercury surface and their detection will depend mainly on adequate data acquisition. A detailed structural analysis, aided by perspective views and large area covering color images, will bring important insights to understand the local tectonic or the volcano/tectonic processes and to detect the possibly associated lithological products.

The linear ridges are minor structures consisting of rounded convex upward ridges, 50–350 km long and 100–1000 m high, cutting intercrater plains and generally following hermean grid. Their age could be comparable to the age of the lobate scarps, but their origin is still strongly debated, since they can be dike-related extrusions or tectonic compressional features.[24] Preliminary simulation have shown the capability of STC to reconstruct 3D morphological shapes with diameters as small as 2 km and elevations as small as 100–150 m (Sec. 3.1).[33] Therefore, an accurate analysis of these features with STC will solve this problem and constrain their stratigraphic age.

3. Stereo Camera Performance

The generation of a high accuracy and high resolution DTM is the main target of the stereo reconstruction by STC. In order to provide the scientific requirements for the optical design and the thermo-mechanical calculations, we simulated the STC performance in DTM generation, taking into account the up to date spacecraft accuracies and the maximum allowed ground spatial scale of 50 m/pixel.

The hypotheses and the estimates reported in the following subsections are preliminary, but important for the definition of some key parameters of the STC design, and will be better defined once synthetic images of Mercury will be available to test algorithms for stereo reconstruction and DTM generation.

3.1. *Precision of the stereo restitution from STC images*

Photogrammetry derives the object point 3D coordinates by spatial intersection of two homologous rays (i.e., rays coming from the same object point). To this aim, the camera perspective center position with respect to the image plane (internal orientation — IO — parameters) must be determined by instrument calibration, while the camera body position and attitude (exterior orientation — OE — parameters) must be determined by image orientation.

The object point precision and accuracy depend on the imaging geometry and on the systematic and random errors affecting calibration, image orientation, and image measurements. Due to the measurement and modeling errors, homologous rays may not intersect exactly; the object point coordinates are computed by a least squares (l.s.) adjustment and the covariance matrix of the l.s. solution provides the precision (i.e., the parameters of the error ellipsoid).

The STC position will be derived by the Mercury Orbiter Radio-science Experiment (MORE) data: to the present knowledge, their predicted accuracy is expected to improve along the mission time, from about 10 m to about 10 cm. The on board star tracker should provide the spacecraft attitude with an accuracy of 2 arcsec. Position and attitude will be referred to a Mercury-centered, Mercury-fixed cartesian frame.

The accuracy of point determination improves increasing the image scale and with the measurement accuracy of the image coordinates. In addition the elevation accuracy improves at large ratios of the

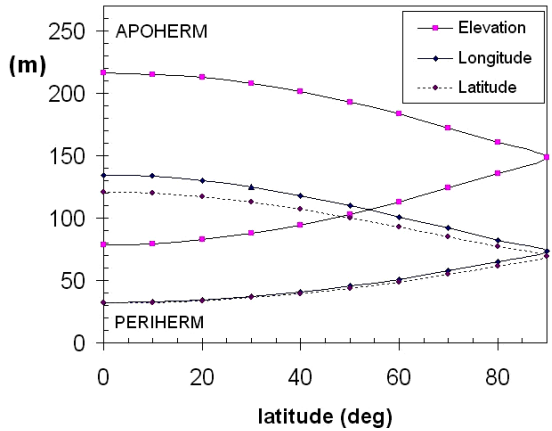

Fig. 1. Precision of point restitution with STC along an half-orbit pass. Both cases at periherm and apoherm are considered.

camera-object distance with respect to the baseline (i.e., the larger the intersection angle between the homologous rays).

Figure 1 reports the precision of the object points along half orbit of the S/C, taking into account the eccentricity of the orbit and the off-nadir angle of the STC channels.

The accuracy of the image coordinates, using image matching algorithms, depends strongly on the local image contrast and distinctness of features. An accuracy of 1 pixel = 10 μm has been conservatively assumed. To assess also the influence of EO. parameters uncertainty, three simulations were executed: (a) with image measurement errors and EO. error-free; (b) with image measurement errors and 10 m error in position; (c) with image measurement errors and with 2 arcsec error in attitude.

Since differences in accuracy among the three simulations turned out to be of a few meters only, it can be concluded that the major error source is the accuracy of image coordinates.

It appears that precision in longitude and latitude are very close to each other and degrade smoothly from about 30 m at the equator to about 70 m at the pole in the periherm arc. With the STC in the apoherm arc the precision decrease continues up to about 130 m at the equator. Precision in elevation has a similar trend, but it is worse and has a stronger degradation rate: from about 80 m at the equator in the periherm arc, precision goes down to about 150 m at the pole and to 215 m at the equator on the apoherm arc.

4. Technical Description

4.1. *Optical design*

The design of the camera has been driven not only by the scientific requirements but also by the aim of saving mass and power. In this attempt an optical solution with common detector and optical elements has been studied for the two channels. The design has been kept as short and compact as possible, with the need of having the possibility to baffle the two channels to cope with straylight problems due to the common optics choice.

The desired 50 m/pixels scale factor at periherm is achieved with the 90 mm system effective focal length, considering the choice of a 10 μm pixel size SiPIN CMOS as detector. This kind of detector is particularly useful both in terms of radiation hardness, given the hostile Mercury environment, and for the capability of snapshot image acquisition, allowing very short exposure times of about 1 msec for STC.

The system consists of a modified Schmidt telescope plus a couple of rhomboid prisms positioned in front of the objective. In that solution, the classical Schmidt correcting plate positioned in the center of the curvature of the spherical mirror has been substituted with a correcting doublet positioned about at half distance, in this way the volume is reduced of about a factor of two with respect to the classical solution. To cope with the field dependent aberrations a two lens field corrector has been placed in front of the detector (see inset of Fig. 2).

All the optical elements, except the rhomboid prisms and the aperture stops (AS), are common to both channels. Common optics, together with the rhomboid prisms are not sensitive to the tilt, make the system free of co-registration error between the channels. Moreover, given the clear separation between the optical path of the two channels, an *ad hoc* baffling system is foreseen and will be studied in detail in the next future.

The global FoV of each channel is $5.3° \times 4.6°$, subdivided into three strips, one for each filter, covering three quasi-contiguous strip on the Mercury surface; at periherm, on the equator, each strip corresponds to an area of about $38 \times 18\,\mathrm{km}^2$ for the panchromatic filter and of about $38 \times 2.2\,\mathrm{km}^2$ for the color ones.

The design has been chosen to satisfy the desired optical performance for all the filters in the whole FoV. The choice of the glasses are restricted to rad-hard glasses, and to have the best performance of transparency the fused silica has been selected for all the dioptric elements. The aperture

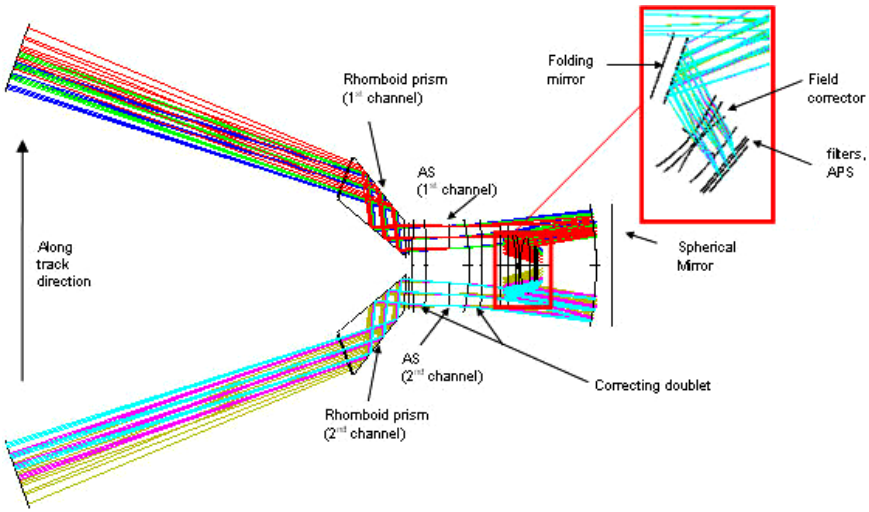

Fig. 2. STC overall optical design layout. Inset shows a zoom of the focal plane region.

stop (AS) position, approximately in the middle of the correcting doublet, has been chosen to allow a good aberration balancing over all the FoV and to make telecentric the system.

To avoid mechanical movable parts, the filter concept is to use different filtering strips deposited contiguously (side by side) on the same substrate. This window will be placed in the converging light beam near the detector. To avoid wavelength shifting due to non-orthogonal incidence of the beam on the filter itself, the camera design has been envisaged to be as telecentric as possible. The optical characteristics of the camera are summarized in Table 1.

4.2. *Mechanical design*

The STC mechanical design is based on the functional and performance requirement derived by the scientific goals with the constraints of a so demanding mission: the high thermal fluxes (10 times the terrestrial solar constant at perihelion) imply the possibility of strong thermal gradients inside the instrument. Moreover, the spacecraft orbit around the planet implies planetary flux that changes from the Sun and eclipse phases, and the planet surface temperature varies from about 100 K to 680 K.

Table 1. STC characteristics.

Optical concept	Catadrioptic: modified Schmidt telescope plus a couple of rhomboid prisms and a field corrector
Stereo solution (concept)	Two identical optical channels; Detector and most of the optical elements common to both channels
Focal length on-axis	90 mm
Pupil size (diameter)	15 mm
Focal ratio	$f/6$
Mean image scale	$23.5''$/pixel (114 μrad/pixel)
FoV (cross track)	5.3°
FoV (along track)	2.4° pancromatic; 0.3° color filters
Detector	SiPIN (2048 × 2048 squared pixel; 10 μm size)
EE	>70% inside 1 pixel
MTF	>60% at Nyquist frequency
Filters	Panchromatic (700 ± 100 nm)
	420 ± 10 nm
	550 ± 10 nm
	700 ± 10 nm
	920 ± 10 nm

Considering the optical layout of STC, the effects of thermal fluxes may induce misalignment of the two stereo channels, providing that they are looking at the planet and the external environment out of phase of 40°.

To minimize this effects the following architecture is implemented: a common subunit STC integrated with VIHI. This architecture, from a conceptual point of view, allows to increase the thermal inertia in such a view that the sub-unit is less sensitive to the thermal transient along the orbits (Fig. 3).

The STC–VIHI unit is mounted on the spacecraft optical bench (O/B): a sandwich structure with aluminum honeycomb core and external layer of CRFP; this interface is mainly structural and a negligible heat flow is foreseen through this interface. Due to the different coefficient of thermal expansion between spacecraft O/B and STC–VIHI structure the thermal distortion must be minimized thanks to kinematics mountings.

The integration of STC and VIHI channels allows to share structural parts minimizing the needed mass; moreover for the thermal aspect, one cold finger at +20°C, placed on the STC side, will remove heat internally generated by the detector and the related thermal electric cooler (TEC), by the proximity electronics and the contribution coming from the environment through the thermal baffling (Fig. 4).

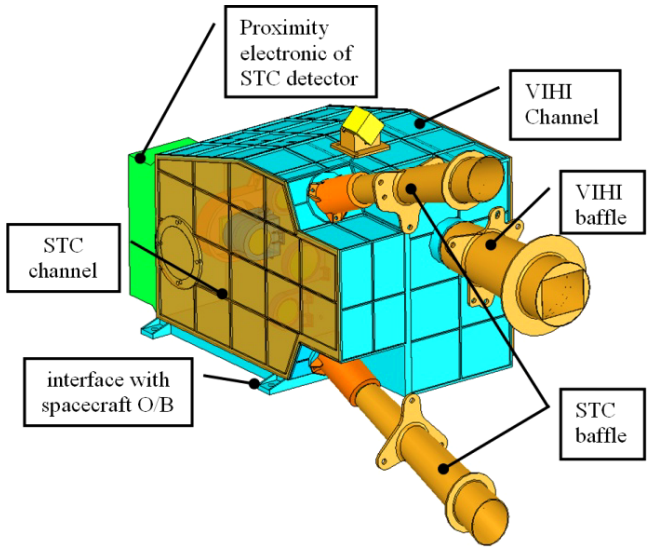

Fig. 3. The mechanical layout of the two channels STC and VIHI.

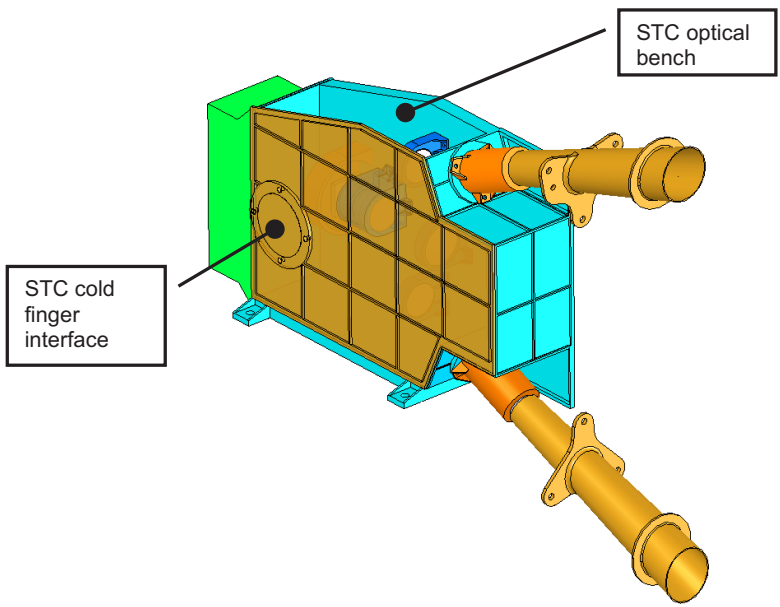

Fig. 4. The STC mechanical layout, the baffles are connected to the spacecraft panel.

5. Operations

The nominal mission will extend over two cycles of 196 days or two Mercury orbital periods, corresponding to a day–night period. In the first six months of the mission, STC has to perform a global mapping of the surface. Therefore, the science observation strategy of STC can be based on a cycle of two orbital periods of 88 days: in one orbital period half of the planet can be studied, then the same observation conditions are repeated on the opposite hemisphere.

To satisfy the scientific requirement of a global mapping with a ground resolution of 50 m at the equator, during the first half of the nominal mission STC must work continuously, to cover with both panchromatic filters the whole surface of the planet. The operative mode that will be used is called *Stereo mapping*; this mode, as a baseline, foresees the use of only two panchromatic filters .

During the second half of the nominal mission, assuming that the global stereo mapping has been completed at least for the 90% of the surface, particularly interesting areas can be mapped using all the possibilities offered by STC. To acquire color pictures on large regions of the Mercury, the *Color mapping mode* will be used; this mode foresees the usage of all the color filters on both STC channels. The stereo mode could be used in this phase to obtain on selected targets a stereo reconstruction with a higher accuracy than the one of the global mapping. For the detailed stereo on small targets a lossless compression ratio (i.e., a compression ratio $\sim$2 on average) will be used, and the maximum overlapping between consecutive tracks.

6. Discussion

The stereo camera for the BepiColombo mission is based on a completely new optical design and acquisition technique, as the push-frame, instead of the push-broom techniques used by HRSC on board the Mars Express mission and the terrestrial satellites SPOT. It is not possible to say which is the best as STC still have to fly to get the first images, but we think we may achieve good results by reducing the number of images to mosaic and having larger single images to find the matching points for the stereo reconstruction.

The Mercury Dual Imager System (MDIS)[40] on board the NASA mission MESSENGER is based on a different approach for the stereo

imaging, as it will use a movable mechanical part allowing to point the same channel at different view angles. Furthermore, the observing strategies are strongly dependent from the different orbits of the spacecrafts.

STC will provide the global mapping at a spatial resolution lower than 110 m/pixel, achieved at the poles, thanks to the low eccentricity orbit of the MPO. While MDIS with the two-cameras strategy will provide a near-uniform global coverage with an average spatial resolution of 140 m/pixel.

References

1. G. Cremonese, A. Sprague, J. Warell, N. Thomas and L. Ksanfomality, *Space Sci. Rev.* **132** (2007) 291–306.
2. R. G. Strom and A. L. Sprague, *Exploring Mercury. The Iron Planet* (Springer in association with Praxis, Cichester, UK, 2003).
3. J. W. Head, C. R. Chapman, D. L. Domingue, S. E. Hawkins, W. E. McClintock, S. L. Murchie, L. M. Prockter, M. S. Robinson, R. G. Strom and T. R. Watters, *Space Sci. Rev.* **131** (2007) 41–84.
4. Y. Langevin, *Planet. Space Sci.* **45** (1997) 31–37.
5. J. Warell, *Icarus*, **156** (2002) 303–317.
6. N. N. Kiselev and D. F. Lupishko, *Solar System Res.* **38** (2004) 85–92.
7. A. L. Sprague, R. W. H. Kozlowski, F. C. Witteborn, D. P. Cruikshank and D. H. Wooden, *Icarus* **109** (1994) 156.
8. D. T. Blewett, B. R. Hawke and P. J. Lucey, *Meteorit. Planet. Sci.* **37** (2002) 1245–1254.
9. A. L. Sprague and T. Rousch, *Icarus* **133** (1998) 174.
10. B. L. Cooper, J. W. Salisbury, R. Killen and A. E. Potter, *J. Geophys Res.* **107** (2002) 101.1029/2000JE001462.
11. A. L. Sprague, J. P. Emery, K. L. Donaldson, R. W. Russell, D. K. Lynch and A. L. Mazuk, *Meteorit. Planet. Sci.* **37** (2002) 1255–1268.
12. J. Warell and D. T. Blewett, *Icarus* **168** (2004) 257–276.
13. J. Warell, A. L. Sprague, J. P. Emery, R. W. H. Kozlowski and A. Long, *Icarus* **180** (2006) 281–291.
14. M. S. Robinson and P. G. Lucey, *Science* **275** (1997) 197–200.
15. M. Sgavetti, L. Pompilio, C. Carli, C. De Sanctis, F. Capaccioni, G. Cremonese and E. Flamini, *Plan. Space Sci.* **55** (2007) 1596–1613.
16. N. J. Trask and J. E. Guest, *J. Geophys. Res.* **80** (1975) 2461–2477.
17. P. D. Spudis and J. E. Guest, *Mercury* (Arizona Univ. Press, 1988).
18. W. F. Bottke Jr., D. D. Durda, D. Nesvorný, R. Jedicke, A. Morbidelli, D. Vokrouhlický and H. F. Levison, *Icarus* **179** (2005) 63–94.
19. R. G. Strom and G. Neukum, *Mercury* (Arizona Univ. Press, 1988).
20. G. Neukum *et al.*, *Planet. Space Sci.* **49** (2001) 1507–1521.
21. R. G. Strom, R. Malhotra, T. Ito, F. Yoshida and D. A. Kring, *Science* **309** (2005) 1847–1850.

22. P. S. Mohit and R. J. Phillips, *J. Geophys. Res.* **111** (2006) 12001, doi: 10.1029/2005JE002654.
23. L. Ksanfomality, G. Papamastorakis and N. Thomas, *Planet. Space Sci.* **53** (2005) 849–459.
24. H. J. Melosh and W. B. McKinnon, The tectonics of Mercury, *Mercury* (Arizona Univ. Press, 1988), pp. 374–400.
25. W. B. McKinnon *Proc. Lunar Planet* (1981).
26. D. Dzurisin, *J. Geophys. Res.* **83** (1978) 4883–4906.
27. H. J. Melosh and Dzurisin, *Icarus* **35** (1978) 227–236.
28. L. Fleitout and P. G. Thomas, *Earth. Planet. Sci. Let.* **58** (1982) 104–115.
29. P. G. Thomas, P. Masson and L. Fleitout, *Mercury* (Arizona Univ. Press, 1988), pp. 401–428.
30. P. H. Schultz and D. E. Gault, *The Moon* **12** (1975) 159–177.
31. G. J. Hostetler and M. J. Drake, *Proc. LPSC* **11** (1980) 1915–1929.
32. S. M. Milkovich, J. W. Head and L. Wilson, *Science* **12** (2002) 259–273.
33. M. Massironi, L. Giacomini, G. Cremonese, M. T. Capria, V. Da Deppo, G. Forlani, G. Naletto, G. Pasquaré and E. Flamini, Simulations using terrestrial geological analogues of the Hermean surface to examine 3D rendering potentialities of the stereoscopic imaging channel of the SIMBIO-SYS package (Bepi-Colombo mission), *Plan. Space Sci.* **56** (2008) 1079.
34. J. A. Burns, *Icarus* **28** (1976) 453–458.
35. H. J. Melosh, *Icarus* **31** (1977) 221–243.
36. B. C. Murray, M. J. S. Belton, G. E. Danielson, M. E. Davies, D. Gault, B. Hapke, B. O'Leary, R. G. Strom, V. Suomi and N. Trask, *Science* **185** (1974) 169–179.
37. T. R. Watters, M. S. Robinson and A. C. Cook, *Geology* **26** (1998) 991–994.
38. P. G. Thomas, *Planet. Space. Sci.* **45** (1997) 3–13.
39. G. Cremonese, M. Bruno, V. Mangano, S. Marchi and A. Milillo, *Icarus* **177** (2005) 122–128.
40. S. E. Hawkins III, J. D. Boldt, E. H. Darlington, R. Espiritu, R. E. Gold, B. Gotwols, M. P. Grey, C. D. Hash, J. R. Hayes, S. E. Jaskulek, C. J. Jr. Kardian, M. R. Keller, E. R. Malaret, S. L. Morchie, P. K. Murphy, K. Peacock, L. M. Prockter, R. A. Reiter, M. S. Robinson, E. D. Schaefer, R. G. Shelton, R. E. Sterner II, H. W. Taylor, T. R. Watters and B. D. Williams, *Space Sci. Rev.* **131** (2007) 247–338.